

Nanoscale Ordered Structure Distribution in Thin Solid Film of Conjugated Polymers: Its Significance in Charge Transport Across the Film and in Performance of Electroluminescent Device

Ming-Chih Chen,[†] Wei-Chun Hung,[†] An-Chung Su,[†] Su-Hua Chen,[‡] and Show-An Chen^{*,†}

Chemical Engineering Department, National Tsing Hua University, Hsinchu, 30013, Taiwan, R.O.C., and
Department of Materials Science and Engineering, National Dong Hwa University,
Hualien 974, Taiwan, R.O.C.

Received: February 23, 2009; Revised Manuscript Received: July 4, 2009

We use ultrahigh-vacuum conducting atomic force microscopy to probe the local current distributions in spin-cast thin films from the solutions of poly(2-methoxy-5-(2'-ethylhexyloxy)-1,4-phenylenevinylene) (MEH-PPV) and poly(9,9-di-*n*-octyl-2,7-fluorene) (PFO). We found that spatially homogeneous distribution of the ordered structures (well-packed chains and/or aggregates) in MEH-PPV can be controlled by the selection of solvent or mixed solvent, by which effects of spatial charge transport distribution in MEH-PPV thin films on the performance of polymer light-emitting diodes (PLEDs) are unambiguously clarified. For PFO thin film, after the treatment by immersing in the mixed nonsolvent composed of a solvent and nonsolvent, the ordered structures (β -phase) are generated; its excess content can result in highly conducting regions. However, the device efficiency can be promoted significantly by optimizing the content of β -phase.

1. Introduction

In the recent decade, the development of conjugated polymers for use as the emitting layer in polymer light-emitting diodes (PLEDs) has been extensive.^{1,2} It is known that the charge transport properties and therefore device performance are highly dependent on morphology of the polymer film,³ because its electrical properties strongly depend on how and to what extent polymer chains interact with one another, which can be tuned extrinsically by controlling orientations of polymer chains and microstructures of the films.^{4–14} However, a correlation among charge transport properties, film morphology, and device performance still remains much to be explored.

Since the thickness of the polymer film is normally about 100 nm or less, a characterization of its charge transport and morphology in nanoscale is necessary. For such purpose, conducting atomic force microscopy (CAFM) is well suited,¹⁵ which can simultaneously measure topography and current distribution with a nanoscale spatial resolution. CAFM has been widely used to map the local electronic properties of organic films under ambient condition or in dry nitrogen atmosphere,^{15–22} but there is no report on using it to image current distribution of polymer thin films in an ultrahigh vacuum (UHV) environment (below 5×10^{-10} Torr), where no adsorbed external molecular layer (such moisture and air) exists. In the UHV environment, interference due to adsorbed molecular layer on film surface and chemical degradation of polymer film during scanning in air can be avoided so that a reliable nanoscale imaging can be achieved.

Indeed, several theoretical reports suggested that an understanding of effects of nanoscale heterogeneity (such as spatial distribution of charge transport) in conjugated polymer thin film could be critical for further development of efficient optoelec-

tronic devices.^{23–25} However, a correlation among nanoscale charge transport distribution, local morphology, and device performance has not been reported yet. In this study, we use UHV-CAFM to probe local current distributions in poly(1-methoxy-4-(2'-ethylhexyloxy)-2,5-phenylenevinylene) (MEH-PPV) spin-cast from solutions in different solvents (or in mixed solvents) and in poly(9,9-di-*n*-octyl-2,7-fluorene) (PFO) spin-cast thin films with minor amount of β -phase structure. The chain alignments that can affect the morphology of MEH-PPV thin film involve arrangements and distributions of one or more of the states: amorphous (isolated chain), crystalline,¹⁴ liquid crystalline,^{26,27} and local ordered structures (well-packed chains,^{28–31} aggregates^{4,8,10,32} and excimer^{4,8,10,32}). The relative amounts of these species and the extent of ordering are found to be sensitive to solvent used for dissolving the polymer,^{4–14,29,32} concentration of solutions,^{4,5,8–11,32} and coating conditions.⁵ For PFO, because of its highly coplanar backbone, a PFO thin film can be physically transformed into a variety of supramolecular structures,^{33–36} such as crystalline phases (i.e., α and α' phases) and noncrystalline phases (such as amorphous, nematic, and β -phase having an extended conjugation length of about 30 repeat units as evidenced by wide-angle X-ray diffraction³⁷). Among these structures, β -phase has attracted extensive attention because of its specific physical properties, such as a lower extent of triplet exciton,³⁸ a reduced ability to be photobleached on the single-molecule scale,³⁹ and efficient energy transfer from the amorphous to β -phase.⁴⁰

Here, we found that homogeneous distribution of the ordered structures (well-packed chains and/or aggregates) in MEH-PPV thin film can be controlled by a selection of solvent in polymer solutions, from which effects of spatial charge transport distribution in MEH-PPV thin films on the performance of PLED are unambiguously clarified. For PFO thin film, excess content of ordered structures (β -phase) can result in highly conducting regions and its device efficiency can be promoted significantly by optimizing the content of β -phase.

* To whom correspondence should be addressed. E-mail: sachen@che.nthu.edu.tw.

[†] National Tsing Hua University.

[‡] National Dong Hwa University.

2. Experimental Methods

2.1. Materials and Substrates. MEH-PPV (its number-average molecular weight (M_n) and polydispersity index are 289 000 Da and 2.19, respectively) was synthesized in accordance with the procedure described previously.⁴¹ The synthetic procedure for PFO end-capped with *p*-*tert*-butylphenyl (TBP) used here is the same as that reported in our previous work.⁴² M_n and polydispersity index of PFO are 245 000 Da and 1.55, respectively. Indium tin oxide (ITO) with a sheet resistance of 8 Ω/\square and glass plate substrates were cleaned sequentially with isopropyl alcohol, acetone, deionized water/ $\text{H}_2\text{O}_2/\text{NH}_4\text{OH}$ (volume ratio = 5:1:1), and deionized water. Then, they were exposed to oxygen plasma at a power of 50 W and a pressure of 200 mTorr for 5 min in a plasma generator chamber with parallel plate electrodes.

2.2. Ultrahigh-Vacuum Conducting Atomic Force Microscopy (UHV-CAFM). The CAFM (RHK, America) was performed under the UHV condition (5×10^{-10} Torr). Rectangular Au tips (CSC-36, NDMDT, Russia) with an estimated spring constant of 0.65 N/m were used in contact mode for simultaneous topography and current measurements. A bias voltage was applied to the tip and the current was measured by a preamplifier (RHK, IVP-300) with gain 10^9 V/A, approximately 500 Hz bandwidth and detection limit below 10 pA. The contact force was maintained at around 20 nN as determined from a force–distance plot. MEH-PPV films (80 nm) for UHV-CAFM measurement were prepared by spin-coating onto ITO glass substrates from 5 mg/mL solutions in chloroform (i.e., CHCl_3), chlorobenzene (CB), their mixtures with the volume ratios of 3:1 and 1:3, and toluene in an Ar glovebox. In order to maintain same film thicknesses, the polymer solutions with chloroform, chlorobenzene (CB), their mixtures with the volume ratios of 3:1 and 1:3, and toluene as solvents were spin-coated at 1100, 800, 1000, 900, and 1000 rpm, respectively. For PFO, its films (80 nm) spin-cast on ITO glass substrates at 1000 rpm from its solution in tetrahydrofuran (THF) (7.5 mg/mL) were dipped in a mixed solvent/nonsolvent (THF/methanol (MeOH)) for different period of times to obtain different contents of β -phase. The thickness of MEH-PPV or PFO films was measured by a Tencor Alpha-Step profilometer. The samples for UHV-CAFM measurement were handled in an argon glovebox and then moved into a desiccator. The whole assembly was taken out from the glovebox, and the samples were then transferred quickly (in less than 10 s in air) to the UHV-CAFM sample loading chamber. Such transferring process can minimize possible contamination on sample surfaces by an exposure to air. Thereafter, the samples were transferred from the sample loading chamber to the UHV main chamber. Before UHV-CAFM measurement, all samples were kept under an ultrahigh vacuum of 5×10^{-10} Torr for 6 h. Furthermore, to avoid artificial influence, we started the hole current and surface roughness measurements by collecting three sets of films for each MEH-PPV and PFO samples. We found only minor differences in the hole current and surface roughness of films that were prepared under identical conditions (the deviations of hole current and surface roughness were small about ± 1 –3% for each sample). Then, for each CAFM image, it represents the result from single scan.

2.3. Device Fabrication. Devices were fabricated as follows. For a bipolar device, a thin layer (about 80 nm) of MEH-PPV or PFO was spin-coated onto ITO substrate (for PFO device, a thin hole injection layer (25 nm) of poly(styrenesulfonic acid)-doped poly(3,4-ethylenedioxythiophene) (PEDOT-PSS) was spin-coated on an ITO substrate and then baked at 140 °C for

1 h in an oven equipped in the glovebox). Finally, a thin layer of calcium (about 5 nm) covered with a layer of aluminum as the cathode were deposited in a vacuum thermal evaporator through a shadow mask at a pressure of less than 10^{-6} Torr. The active area of the diode is about 6 mm². For a hole-only device, the procedures were the same as those used for a bipolar device based on MEH-PPV except that a thin layer (5 nm) of gold was deposited to replace the calcium layer. Device performances in terms of current–voltage–luminance were characterized by Keithley 238 source measurement unit and Topcon BM-8 luminance meter. To ensure that the differences in device performance were not artifactual, we fabricated and tested five sets of devices for each MEH-PPV and PFO films in our study. We found only minor differences in the performance that were prepared under identical conditions (the deviations of device performance were small within $\pm 5\%$ for each device).

2.4. Grazing-Incidence Wide-Angle X-ray Scattering (GI-WAXS), Ultraviolet–Visible Absorption, and Photoluminescence Spectroscopy. A Bede D1 HR-XRD diffractometer (equipped with a copper target for $\text{K}\alpha$ line of wavelength 0.154 nm, polycapillary collimator/lens, and parabolic multilayer mirrors) was used under a step-scan rate of 0.05° per 5 s in the scattering angle range of 3°–37° (grazing incidence angle 1°). Full range calibration of the scattering angle was made using both silicon and silver behenate standards. Ultraviolet–visible (UV–vis) absorption spectra were measured by using a UV–vis–near-IR spectrometer (Perkin-Elmer, Lambda 19). PL spectra were measured by using a fluorescence spectrometer (FluoroMAX-3 from Jobin Yvon). To prepare specimens for GI-WAXS, UV–vis absorption, and PL investigations, a thin layer (80 nm) of MEH-PPV was spin-coated onto glass plate from 5 mg/mL solutions in CHCl_3 , CB, their mixtures with the volume ratios of 3:1 and 1:3, or toluene; PFO films used in UV–vis absorption measurements were spin-coated onto glass plates from its solution in THF and then followed the dipping procedures as described in section 2.2.

3. Results and Discussion

3.1. Effect of Solvent on Spatial Homogeneity of Ordered Structures, Charge Transport, and Device Performance in MEH-PPV Films. **3.1.1. CAFM and Electrical Characteristics Studies.** For MEH-PPV, films were prepared from its solutions (5 mg/mL) in various solvents by spin-casting on ITO substrate in an argon glovebox and their CAFM images (with a tip bias of +7 V) of topography and current simultaneously acquired during scanning are shown in Figure 1. The solvents used involve CHCl_3 , CB, their mixtures with the volume ratios 3:1 and 1:3, and toluene. These thin films with a thickness of about 80 nm are designated as CHCl_3 film, CB film, 75% CHCl_3 film, 25% CHCl_3 film, and toluene film, respectively. 75% CHCl_3 film and 25% CHCl_3 film are also designated as mixed-solvent films in some occasions. The topographical R_{ms} (root-mean-square roughness) values for these films are 1.63, 1.59, 1.53, 1.46, and 1.61 nm, respectively, indicating that their surface roughness are similar. Moreover, no topographical change was observed after repeated current image scanning for all the film samples, indicating an absence of electrochemical reaction during the scanning. This guarantees the quality and reproducibility of measurements in this study, which can be attributed to the UHV environment during the CAFM scanning.

In the current images, high-current regions have sizes ranging from 15 to 200 nm, as verified from the cross-section analysis and to be revealed in details later. The tip–sample contact

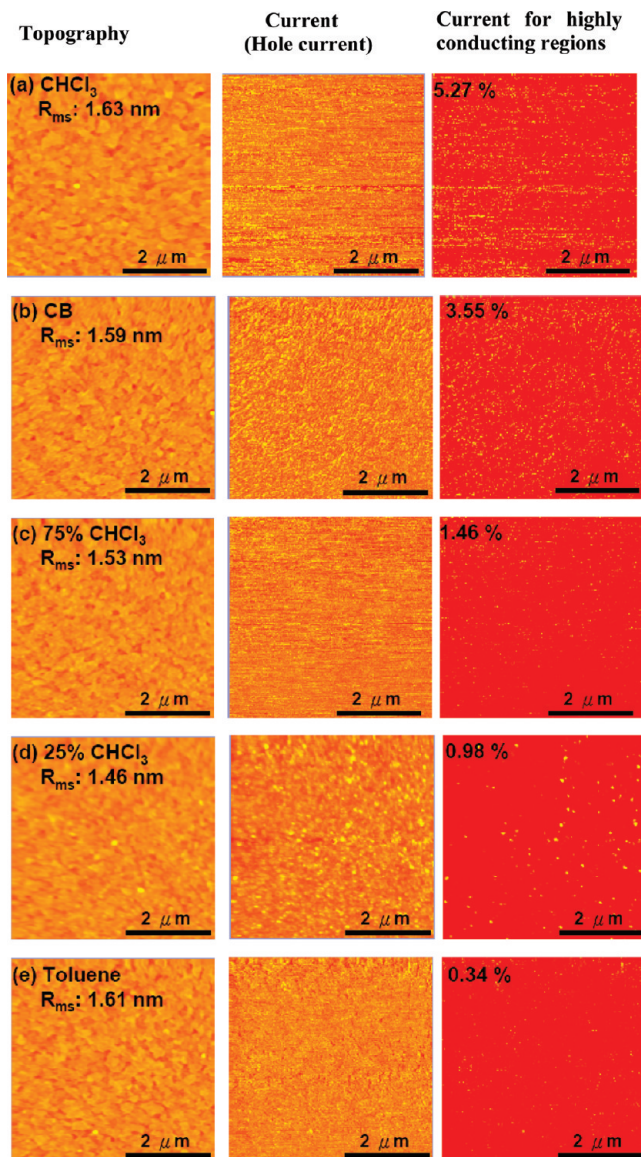


Figure 1. CAFM images of topography, current, and current for highly conducting regions: (a) CHCl_3 , (b) CB, (c) 75% CHCl_3 , (d) 25% CHCl_3 , and (e) toluene films (spatial coverage of images: $4.5 \times 4.5 \mu\text{m}^2$; thickness of MEH-PPV films: 80 nm).

diameter is estimated by the Hertz model⁴³ to be ca. 12 nm,⁴⁴ which is close to the experimental observation and also ensures that the electric field exists primarily in the region defined by tip-sample contact. The characteristic parameters including the average hole currents, standard deviations, and relative standard deviations of average hole current for current images in Figure 1 are listed in Table 1. Figure 2 shows the histograms for the current images (65 536 data points in the current image of $4.5 \times 4.5 \mu\text{m}^2$), which can serve as an index for the homogeneity of current images in Figure 1.¹⁵ Since an Au-coated AFM tip is used as the probe and a positive voltage is applied on it, the current is mainly contributed by holes (Au and ITO have work functions of around 5.1 and 5.0 eV, respectively, both are close to the HOMO level of MEH-PPV, 5.0 eV, but depart from the LUMO level, 2.9 eV).⁴⁵

Note that the standard deviations and the relative standard deviations of hole current for 75% CHCl_3 , 25% CHCl_3 , and toluene films are lower than those for CHCl_3 and CB films (Table 1), which indicates that 75% CHCl_3 , 25% CHCl_3 , and toluene films have a more homogeneous morphology for hole

TABLE 1: Average Hole Currents and Relative Standard Deviations Extracted from Current Images in Figure 1

sample	av hole current I_{av} (nA) ^a	std dev I_{rms} (nA) ^b	rel std dev (%) ^c
CHCl_3 film	0.393	0.228	58
CB film	0.399	0.187	47
75% CHCl_3 film	0.149	0.054	36
25% CHCl_3 film	0.175	0.051	29
toluene film	0.438	0.128	29

^a The average hole current of the measurement (65536 data points in the current image of $4.5 \times 4.5 \mu\text{m}^2$). ^b Standard deviation is a root mean square of the hole current ($I_{\text{rms}} = (\sum(I_i - I_{\text{av}})^2/n)^{1/2}$). ^c Relative standard deviation is equal to $I_{\text{rms}}/I_{\text{av}}$; a smaller value indicates more homogeneous morphology for hole carrier conduction.

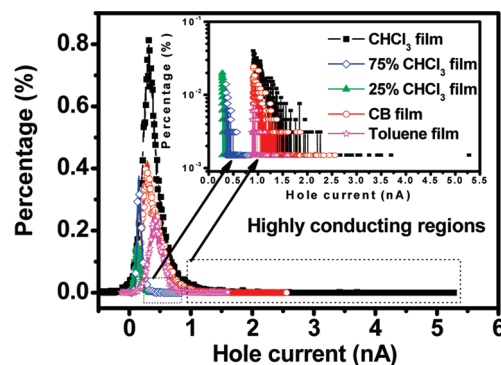


Figure 2. Histograms of the current images in Figure 1. The inset shows the current distributions for highly conducting regions.

carrier transport. It means that the pathways for charge carriers between the anode and cathode are more spatially homogeneous for these films. In contrast, CHCl_3 and CB films have relatively inhomogeneous morphology for hole carrier transport. Conformations of polymer chains in thin solid films prepared by spin coating are usually not in a thermodynamic equilibrium state due to the high rate of solvent evaporation along with radial direction flow associated with this method. For the difference in homogeneity of nanoscale current distribution, one could argue that it resulted from a different volatility of the solvents used. However, volatility of toluene (boiling point = 111 °C; vapor pressure at 20 °C = 22 mmHg) and mixed solvents (CHCl_3 mixed with CB) lie in between those of CHCl_3 (boiling point = 61 °C; vapor pressure at 20 °C = 159 mmHg) and CB (boiling point = 132 °C; vapor pressure at 20 °C = 8.8 mmHg), but are not the lowest or highest among them. Therefore, volatility of toluene and mixed solvent is not the main source for more spatially homogeneous morphology for charge carrier transport.

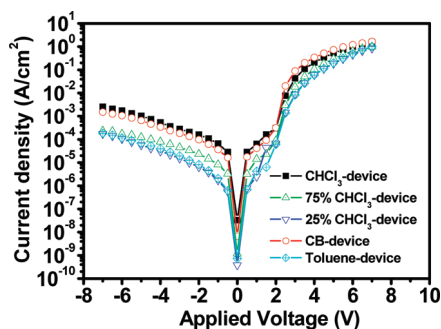
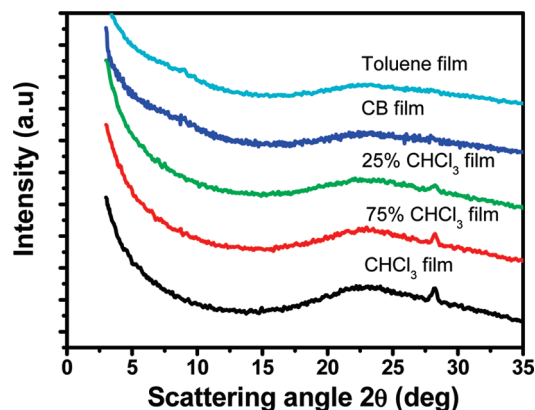
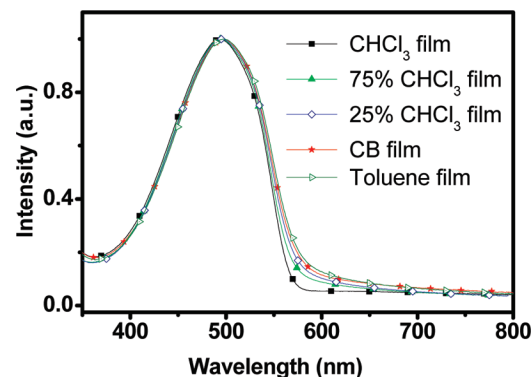
To explore effects of the extent of homogeneity in current distribution in MEH-PPV thin films on performance of the corresponding PLEDs, devices with the structure ITO/MEH-PPVs(80 nm)/Ca/Al were fabricated. The devices with CHCl_3 , CB, 75% CHCl_3 , 25% CHCl_3 , and toluene films are designated as CHCl_3 -device, CB-device, 75% CHCl_3 -device, 25% CHCl_3 -device, and toluene-device, respectively. 75% CHCl_3 -device and 25% CHCl_3 -device are also designated as mixed-solvents-devices in some occasions. The characteristics of the devices are summarized in Table 2 (curves for device performance are shown in Figure S1 in the Supporting Information). 75% CHCl_3 -device, 25% CHCl_3 -device, and toluene-device have higher efficiency than CHCl_3 -device and CB-device by a factor of about 2. Figure 3 shows the current density-electric field curves for these devices. The rectification ratio (ratio of currents at ± 7 V)

TABLE 2: Performance of MEH-PPV Devices Prepared from Solutions in Different Solvents (Device Structure: ITO/MEH-PPVs/Ca/Al)

device	max efficiency (cd/A)	max brightness (cd/m ²)	current density at −7 V (A/cm ²)	rectification ratio at ±7 V
CHCl ₃ film	1.3 (4.5 V)	16992 (7 V)	2.6×10^{-3}	590
CB film	1.6 (4 V)	17347 (7 V)	1.5×10^{-3}	1099
75% CHCl ₃ film	3.2 (4.5 V)	19998 (7 V)	2.4×10^{-4}	4125
25% CHCl ₃ film	3.4 (4.5 V)	20931 (7 V)	1.7×10^{-4}	4941
toluene film	2.6 (4 V)	21482 (7 V)	1.8×10^{-4}	5435

of 75% CHCl₃-device (4125), 25% CHCl₃-device (4941), and toluene-device (5435) are higher than that of CHCl₃-device (590) and CB-device (1099) by a factor of about 5–9. In the operation of reversed bias (at an applied voltage of −7 V), the current densities of 75% CHCl₃-device (2.4×10^{-4} A/cm²), 25% CHCl₃-device (1.7×10^{-4} A/cm²), and toluene-device (1.8×10^{-4} A/cm²) are lower than those of CHCl₃-device (2.6×10^{-3} A/cm²) by factors of 10.8, 15.3, and 14.4 and CB-device (1.5×10^{-3} A/cm²) by factors of 6.3, 8.8, and 8.3, respectively, indicating significantly larger current leakages in the latter two devices. The presence of leakage current reflects that the forward current could flow across the device without contributing to light emission, resulting in an energy loss and lower luminance efficiency.^{46–48} Hence, the suppression of current leakage is an important factor to elevate the efficiency of PLED devices, as revealed by the superior performance of 75% CHCl₃-device, 25% CHCl₃-device, and toluene-device in this study. This part is often neglected in the literature.

Further discussion on the origin of leakage current is given as follows. If we define the area with a local hole current 2 times larger than the average hole current as the “highly conducting region”, the percentage of coverage of the highly conducting regions on the CHCl₃, CB, 75% CHCl₃, 25% CHCl₃, and toluene films are 5.27%, 3.55%, 1.46%, 0.98% and 0.34%, respectively (current images for highly conducting regions in Figure 1 and the inset in Figure 2). The highly conducting regions for all the five films distribute randomly in the films. And their sizes range from 50 to 200 nm (as determined by cross-section analysis on current images for highly conducting regions) regardless of the solvent used, which are comparable to the thickness of MEH-PPV film in the devices (~80 nm). Moreover, the sums of individual hole current of the highly conducting regions in 75% CHCl₃ film (32.2 μ A), 25% CHCl₃ film (26.7 μ A), and toluene film (21.5 μ A) are lower than that in the CHCl₃ film (362.6 μ A) by factors of 11.3, 13.6, and 16.9 and that in the CB film (228.9 μ A) by factors of 7.1, 8.6, and 10.6, respectively. This trend is close to the results obtained from the measurement of leakage current at the applied voltage −7 V in Figure 3 and listed in Table 2, in which the current

**Figure 3.** Current density–voltage curves of the bipolar devices: ITO/MEH-PPVs(80 nm)/Ca(5 nm)/Al(100 nm).**Figure 4.** GI-WAXS data measured in the perpendicular direction of the MEH-PPV films. The spacing corresponding to the peak at $2\theta = 28^\circ$ is 0.32 nm.**Figure 5.** UV–vis absorption spectra of the MEH-PPV films prepared by spin-casting from its solutions in various solvents and mixed solvents.

densities of 75% CHCl₃-device, 25% CHCl₃-device, and toluene-device are lower than that of CHCl₃-device by factors of 10.8, 15.3, and 14.4 and that of CB-device by factors of 6.3, 8.8, and 8.3, respectively. Therefore, the highly conducting regions can be considered as the “leakage spots” (current flows preferentially through these spots) in the MEH-PPV thin films, which increase the probability of electrical shorts and thus become origins of current leakage in PLEDs. As a result, the lower leakage current in 75% CHCl₃-device, 25% CHCl₃-device, and toluene-device can be attributed to the less coverage of highly conducting regions, which could be due to their more spatially homogeneous morphology for charge carrier conduction (smaller standard deviation and relative standard deviation as shown in Table 1). The difference in the extent of current leakage should not result from a difference in surface roughness, since the R_{ms} values of all the films are similar.

3.1.2. GI-WAXS and UV–Vis Absorption Studies. To further reveal the origin of highly conducting regions, all the films (onto glass plates) were analyzed by GI-WAXS and UV–vis absorption spectroscopy as shown in Figures 4 and 5, respectively. No sharp scattering peak is observed in the GI-WAXS data, indicating a lack of crystalline structure for all the samples. However, the substantial halos at $2\theta = 28^\circ$ are observed in CHCl₃, 75% CHCl₃, and 25% CHCl₃ films, indicating that nanodomains with a characteristic spacing of 3.2 Å (the corresponding Bragg-like characteristic d spacing) are embedded in the amorphous matrix of these three films. Such a spacing has been assigned to the “interchain stacking” in the conjugated polymers, poly(*p*-phenylenevinylene) (PPV),³¹ MEH-PPV,^{14,49} and poly(2,3-diphenylphenylene) (DP-PPV).⁵⁰

Note that such stacking in DP-PPV powder can neither be disrupted by heating up to 330 °C nor be solvated by chloroform.⁵⁰ Therefore, nanodomains in the present CHCl_3 , 75% CHCl_3 , and 25% CHCl_3 films are expected to have high stability. As the volume ratio of CB increases, the scattering intensities of peak at $2\theta = 28^\circ$ of the films decrease. Therefore, the fractions of nanodomains in the MEH-PPV films can be expected to decrease in the order CHCl_3 film > 75% CHCl_3 film > 25% CHCl_3 film. Nanodomains are absent in CB and toluene films as demonstrated by the absence of the scattering peak at $2\theta = 28^\circ$. The presence of such nanodomains could affect charge transport since the distribution and orientation of the nanodomains were found to be critical to the field-effect mobility of regioregular polythiophene films.^{51–53} Nonetheless, no report on effects of nanodomains on the charge transport behavior in MEH-PPV thin films is given in the literature. Thus, it is expected that the existence and distribution of the nanodomains should play a dominant role on charge carrier transport in CHCl_3 , 75% CHCl_3 , and 25% CHCl_3 films. The detailed properties of the nanodomains are discussed in the following section.

In addition to nanodomains discussed above, aggregates (a ground-state absorption and emission species formed by inter-segmental π – π stacking in conjugated polymers as to be revealed in more detail below)^{4,8–11} also play an important role on the charge transport properties of conjugated polymers. Figure 5 shows UV–vis absorption spectra of the five films. The absorbance of the long-wavelength tail (>580 nm), which is caused by the absorption of aggregates,^{4,8–11} increases in the order of CHCl_3 film \ll 75% CHCl_3 film < 25% CHCl_3 film < CB film < toluene film. Therefore, the content of aggregates should also increase in the same sequence. The detailed properties of aggregates are discussed in the following section.

3.1.3. The Properties of Nanodomains and Aggregates.

Aggregates are the new ground-state “interchain” species formed between adjacent conjugated segments by extending the π -delocalization system. Therefore, both the absorption and emission regions of aggregates are lower in energy than those of the independent chain segments. According to Nguyen et al.,^{4,8,9} MEH-PPV chains in aromatic solvent (such as CB, toluene) take an open and extended conformation, thereby facilitating the formation of aggregates. Upon spin-casting from its solutions, aggregates formed in the solution can survive to some extent so that aggregates can be preserved in the film. On the contrary, MEH-PPV chains in nonaromatic solvent (such as THF, CHCl_3) take a compact conformation so that the formation of aggregates is not facilitated. After spin-casting, intrachain species dominate in the film. Thus, MEH-PPV film from aromatic solvents has more aggregates than those from non-aromatic solvents. Moreover, from our GI-WAXS data (Figure 4), the nanodomains are absent in CB and toluene films. Therefore, the nanodomains in CHCl_3 film must not be aggregates.

In addition, photophysical properties and structures of well-packed independent chains (the chain segments are compactly stacked without ground-state interaction) and aggregates in PPV-based polymers have been reported in our previous works,^{28,54} in which energy transfer from isolated chains and well-packed chains to aggregates were observed. The PL emission of well-packed chains is well structured and characteristic of isolated-chain luminescence, indicating the absence of ground-state interaction and the independence of these segments in the assemblies.^{28,29} On the contrary, aggregates show structureless emission profile.^{4,8,9,28,54}

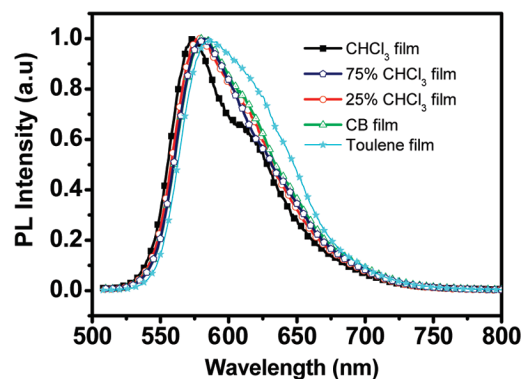


Figure 6. Normalized PL spectra of the MEH-PPV thin films.

The emission characteristics of well-packed chains can be demonstrated by the model polymer, poly(*p*-phenylenevinylene) (PPV). PPV is crystalline and has considerably good intrachain order.^{55,56} At normal atmospheric pressure, adjacent PPV chains are slipped relative to each other so that overlap of π -orbitals between chains is not possible, even though the nearest distance between them is as short as ~ 0.3 nm.³¹ This value is very similar to the characteristic spacing of the nanodomains in CHCl_3 film (0.32 nm, as shown in Figure 4). In addition, Figure 6 shows that CHCl_3 film gives a weak shoulder (620–660 nm) than CB and toluene films (CHCl_3 film has an emission spectrum with vibronic structures), indicating that the PL emission of the CHCl_3 film is similar to characteristic of isolated-chain luminescence more than that of the CB and toluene films. Furthermore, CHCl_3 film also shows weaker ground-state interaction [weaker absorbance of long wavelength edge (>580 nm)] than CB and toluene films (Figure 5), and the nanodomains are absent in CB and toluene films (Figure 4). As a result, we can infer that the nanodomains in CHCl_3 film could be similar to well-packed independent chains, not aggregate. The origin of well-packed chains in CHCl_3 film is not fully understood at the present stage. However, it could be resulted from a rapid evaporation of the volatile solvent CHCl_3 and applied centrifugal force during spin-coating. Further investigation for the origin of well-packed chains in MEH-PPV thin films is on the way.

3.1.4. Schematic Diagrams of Spatial Distribution of Ordered Structures in Films Prepared by Use of Various Solvents and Mixed Solvents.

Film Prepared by CHCl_3 and CB as Solvents. A correlation between the structural information (Figures 4 and 5) and the presence of highly conducting regions (Figures 1 and 2 and Table 1) is depicted in Figure 7, which provides a cartoon depiction of distribution of the ordered structures. For CHCl_3 film, the formation of highly conducting regions can be attributed to the spatially inhomogeneous distribution of the nanodomains, which offer percolated pathways for charge transport across the film as illustrated in Figure 7a. Thus, current can preferentially flow through these percolated pathways, which increase the extent of electrical shorts in these paths and lead to an increase of leakage current. The variation in the extent of current of highly conducting regions in CHCl_3 film should result from a variation in the extent of percolation. In contrast, it is not the case for CB film since it does not contain nanodomains (Figure 4) but aggregates (Figure 5). Thus, most of the highly conducting regions in CB film must be related to the percolated pathways formed by aggregate-rich regions, through which current also preferentially passes to generate local higher current density, as illustrated in Figure 7b. Since toluene film and mixed-solvents films (75% CHCl_3 film and 25% CHCl_3 film) have relatively homogeneous morphology for carrier transport (Figures 1 and 2 and Table 1), the distribution of

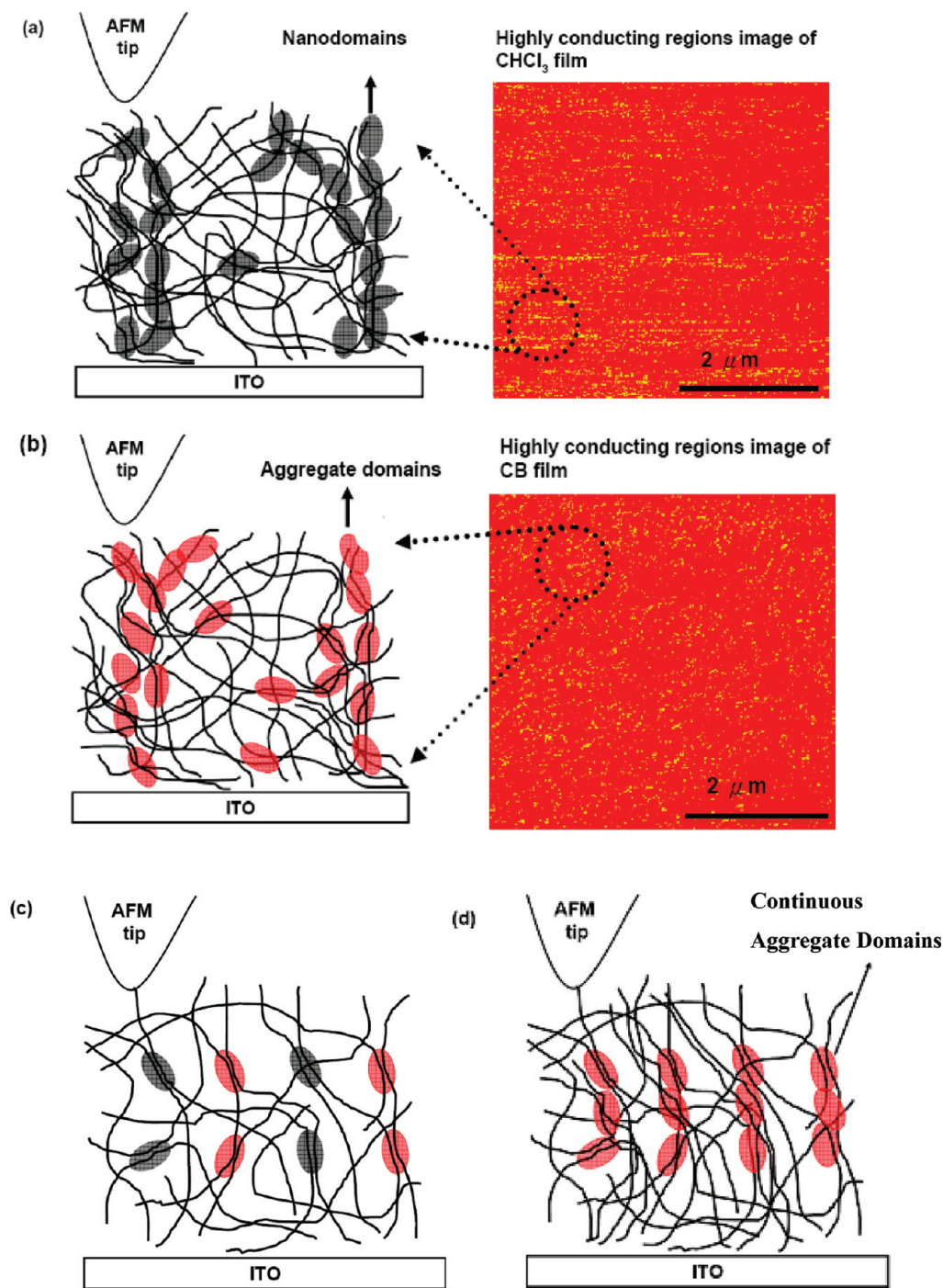


Figure 7. Schematic diagrams of MEH-PPV morphology in the thin films prepared by use of various solvents: (a) CHCl_3 film, (b) CB film, (c) mixed-solvent film, and (d) toluene film. In (a) and (b), inhomogeneous paths formed by ordered domains with close contacts for carrier conduction are shown. In (c) and (d), relatively homogeneous paths for carrier conduction are shown in which the ordered domains are more or less isolated or low extent of contact, respectively. Gray ellipses and red ellipses stand for nanodomains and aggregates, respectively.

aggregates in toluene film or nanodomains/aggregates in mixed-solvent films must be relatively more homogeneous. However, there are still a coverage of the highly conducting regions in toluene film or mixed-solvent films, which must also be related to the aggregate-rich regions or nanodomains/aggregates-rich regions as to be revealed in the following section.

It has been reported that the presence of more aggregates in MEH-PPV thin film can lead to better carrier transport properties (higher carrier mobility and/or more carrier injection)^{4,6–10,32} but poor luminescence efficiency because of quenching of excitons by aggregates.^{4,8–10,32,57,58} They suggested that these two factors can lead to a fundamental trade-off in optimizing film morphol-

ogy for device performance. MEH-PPV film cast from a solution in aromatic solvent, such as CB, dichlorobenzene, and toluene, can induce more aggregates than that in nonaromatic solvent (CHCl_3 and THF).^{4,6–10,32} Nguyen et al.^{4,8–10,32} showed that PLEDs based on MEH-PPV film spin-cast from THF have higher device efficiency than those based on MEH-PPV films spin-cast from CB, suggesting that the quenching of excitons due to the presence of more aggregates play a dominant role over the enhanced charge transport properties. This result is contrary to the reports by Sinha et al.¹¹ and Liu et al.,^{6,7} who found that PLEDs based on MEH-PPV film spin-cast from CB have higher device efficiency than those spin-cast from THF.

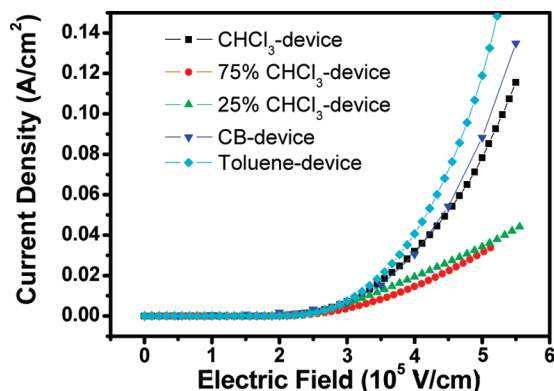


Figure 8. Current density–electric field curves of the hole-only devices: ITO/MEH-PPVs(80 nm)/Au(5 nm)/Al(100 nm).

In other words, a correlation among the quenching of excitons by aggregates, charge transport properties, and device performance is still ambiguous. Therefore, we will not discuss the effect of these two factors on device performance in this paper. However, as revealed from the UHV-CAFM, GI-WAXS, UV–vis absorption spectra, and device performance results (Figures 1–5 and Tables 1 and 2), we found that the spatial distribution of the ordered structures (aggregates and/or nanodomains) in MEH-PPV thin films (Figure 7) is another important factor that affects device performance. The more spatially homogeneous distribution of ordered structures (aggregates and/or nanodomains) in MEH-PPV thin film (smaller relative standard deviation shown in Table 1) can result in less coverage of highly conducting regions (Figure 1), which leads to a lower current leakage in the corresponding device with optimal device efficiency (Table 2). Moreover, by using near-field scanning probe microscopy (NSOM), Nguyen et al.,^{10,59} Huser et al.,⁶⁰ and our groups^{61,62} found that the spatial homogeneity of MEH-PPV film can be greatly affected by annealing or casting from some solvents. However, these works did not provide a direct correlation among homogeneity of spatial charge transport distribution in MEH-PPV thin film, distribution of local ordered structure, and device performance.

Films Prepared by Mixed Solvents and Toluene as Solvents.

At this stage, though the origin of spatially homogeneous morphology for charge carrier transport in 75% CHCl₃ film, 25% CHCl₃ film, and toluene film still cannot be solidly clarified, it is reasonable to expect that the chemical structure of solvent does contribute to the present results. Since toluene or mixed solvents (chloroform mixed with chlorobenzene) have both aliphatic (methyl) and aromatic (phenyl) moieties, both the alkyl side chains and aromatic backbones of MEH-PPV are expected to be well solvated by toluene or mixed solvents,^{4–11} resulting in chain conformations with no preferential solvation and thus a relatively homogeneous morphology. In order to further understand the spatial distribution of ordered structures in mixed-solvent films and toluene film, we fabricated the hole-only devices [ITO/MEH-PPVs(80 nm)/Au/Al], for which their hole current density versus electric field (J – E) characteristic curves are shown in Figure 8. At the same electric field, the devices with mixed-solvent films show lower hole current density than those with CHCl₃ and CB films. Furthermore, it should be emphasized that the highest occupied molecular orbital (HOMO) of these MEH-PPV films is independent of the solvent used (5.0 eV for all the films as determined by ultraviolet photoelectron spectroscopy), indicating that the hole-injection barrier is the same for these five films. Thus, the lower hole current for the devices with mixed-solvent films are due to lower hole mobility in mixed-solvent films.

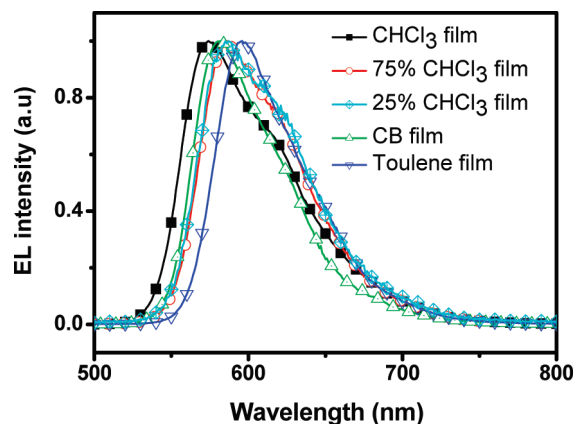


Figure 9. Normalized EL spectra for the device ITO/MEH-PPVs/Ca/Al.

On the basis of the above-mentioned results and descriptions, we propose the reasons for the greatly decreased hole mobility in mixed-solvent films and infer the spatial distribution of ordered structures in these films as follows. As revealed from the UHV-CAFM results (Figures 1 and 2 and Table 1), mixed-solvent films should have more spatially homogeneous distribution of the nanodomains and aggregates than CHCl₃ and CB films (Figures 4 and 5). Thus, charge carrier mobility may be hindered by more random distribution of ordered regions (nanodomains and aggregates) in disordered (isolated chains) regions in mixed-solvent films relative to those in CHCl₃ and CB films. Moreover, these ordered regions (the nanodomains and aggregates) may also act as charge traps (the bandgap of nanodomains and aggregates lie within the bandgap of isolated chain).^{29,63} As a result, the hopping of charge carriers in mixed-solvent films is slowing down. This issue is illustrated in Figure 7c for clarity.

One may expect that toluene film should have lower hole mobility than mixed-solvent films, since toluene film has more aggregates (Figure 5) than mixed-solvent films. However, we found that the hole current density of the device with toluene film is higher than that of the devices with mixed-solvent films (Figure 8). A possible explanation is that the presence of more aggregates in toluene films facilitates the formation of continuous aggregates domains and thus reduces the hopping distances of charge carrier between ordered (aggregates) and disordered (isolated chains) regions. This issue is schematically illustrated in Figure 7d for clarity. However, continuous aggregates domains in toluene film may also act as charge traps.

3.1.5. Effect of Mixed Solvents on Device Performance. In order to understand the higher performance for mixed-solvents-devices, we fabricated the bipolar devices [ITO/MEH-PPVs(80 nm)/Ca/Al] to evaluate the electroluminescent (EL) spectra. Figure 9 shows the normalized EL spectra for all the five films (CHCl₃-device, CB-device, 75% CHCl₃-device, 25% CHCl₃-device, and toluene-device) are normalized at their emission maxima at 3 V. The wavelengths at the highest intensity ($\lambda_{\text{max},s}$) in EL spectra are red-shifted in the increasing order of CHCl₃-device (574 nm) < CB-device (582 nm) < 75% CHCl₃-device (586 nm) < 25% CHCl₃-device (587 nm) < toluene-devices (596 nm). As can be seen, the $\text{EL}\lambda_{\text{max},s}$ of mixed-solvents-devices are more red-shifted than those of CHCl₃-device and CB-device. This observation implies that spatially homogeneous distribution of nanodomains and aggregates in mixed-solvent films can act as charge traps and recombination centers at which both hole and electron prefer to recombine and lead to a more effective utilization of charge carrier and therefore higher device ef-

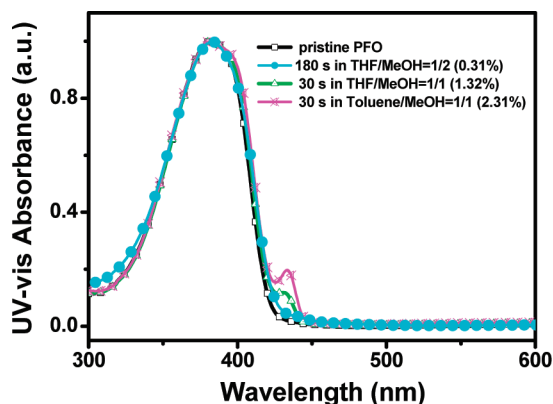


Figure 10. UV-vis absorption spectra of pristine PFO film dipped in the mixed nonsolvents, THF (solvent)/ MeOH (nonsolvent) at the volume ratio 1:2 for 180 s and at the volume ratio 1:1 for 30 s, and in the mixed nonsolvent, toluene (solvent)/MeOH (nonsolvent) at the volume ratio 1:1 for 30 s.

iciency. As a result, in addition to lower leakage current in mixed-solvents-devices, homogeneous distribution of nanodomains and aggregates acting as charge traps and recombination centers is another important factor to affect the efficiency, as illustrated schematically in Figure 7c. Note that the spatially inhomogeneous distribution of the nanodomains or aggregates in CHCl_3 film or CB film offer percolated pathways for charge transport across the film. Thus, the current can preferentially pass through these percolated pathways, which result in a lower probability for carriers to recombine and lead to a larger current leakage in CHCl_3 -device or CB-device and therefore lower device efficiency.

3.2. Relationship between Spatial Homogeneity of Ordered Structures and Device Performance in PFO Films.

3.2.1. CAFM Study. For the other category of conjugated polymer, PFO, the ordered structure that can be generated after a post treatment of its thin film is β -phase, which has a well-packed structure with a conjugation length of 30 repeat units as estimated by theoretical calculation by Grell et al.³⁷ Here UHV-CAFM is also used to map nanodomain current distribution. The formation of the β -phase in PFO thin film was carried out by dipping PFO films spin-coated on ITO substrate (termed as pristine PFO) in the mixed nonsolvents [THF(solvent)/MeOH(nonsolvent) at the volume ratios 1:1 and 1:2 and toluene/MeOH at the volume ratio 1:2] for various periods of time from 30 to 180 s,⁶¹ during which no appreciable dissolution of PFO was observed and the β -phase was found to generate at the content up to 2.31%, as estimated from the area fraction of the UV-vis absorption characteristic peak at 430 nm from spectral deconvolution (Figure 10).⁴⁰ The corresponding contents of β -phase so generated are 0.31%, 1.32%, and 2.31% and designated as β -PFO(0.31%), β -PFO(1.32%), and β -PFO(2.31%) films, respectively.

With a tip bias of +10 V, the topography and current images simultaneously acquired during scanning are shown in Figure 11 for pristine PFO, β -PFO(0.31%), β -PFO(1.32%), and β -PFO(2.31%) films. And the topographical R_{ms} (root-mean-square roughness) values for these films are 0.83, 1.13, 2.12, and 2.36, respectively, indicating that the surface roughness increases with increasing β -phase content. In the current images, if we define the area with a local current larger than 15 pA as the “highly conducting region” (the area with a local current below 15 pA is defined as “nonconducting region” since the noise range of background current for PFO thin films measurement is about 10 ± 2 pA), the percentages of coverage of the

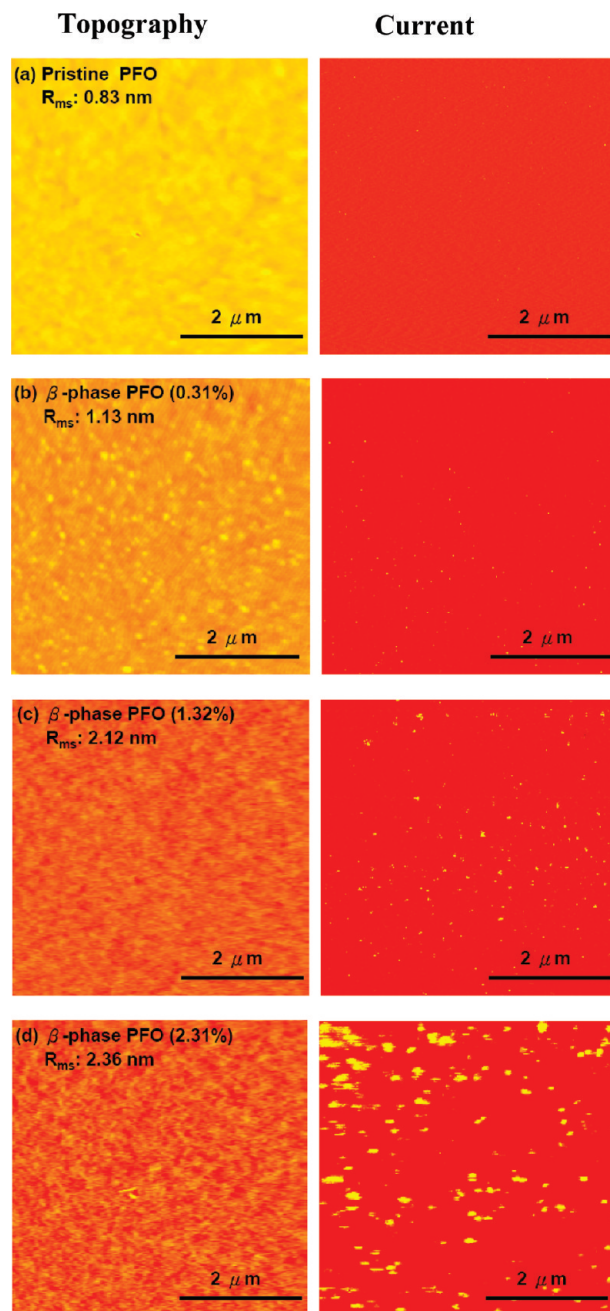


Figure 11. CAFM images of topography and current: (a) pristine PFO, (b) β -PFO (0.31%), (c) β -PFO (1.32%), and (d) β -PFO (2.31%) films (spatial coverage of images: $5.0 \times 5.0 \mu\text{m}^2$; thickness of PFO film: 80 nm).

highly conducting regions on pristine PFO, β -PFO (0.31%), β -PFO (1.32%), and β -PFO (2.31%) films are 0.05%, 0.26%, 1.46%, and 2.74%, respectively, which are close to the total β -phase content estimated from the area fraction of the UV-vis absorption characteristic peak at 430 nm (Figure 10). Furthermore, since an Au-coated AFM tip was used as the probe and

TABLE 3: Performance of the Devices ITO/PEDOT-PSS/PFs/Ca/Al

device	max efficiency (cd/A)	max brightness (cd/m ²)	current density at -3 V (A/cm ²)
pristine PFO	1.2 (5 V)	848 (9 V)	8.3×10^{-6}
β -PFO (1.32%)	2.9 (5 V)	1557 (9V)	3.7×10^{-5}
β -PFO (2.31%)	1.5 (6.5 V)	2778 (9V)	9.1×10^{-4}

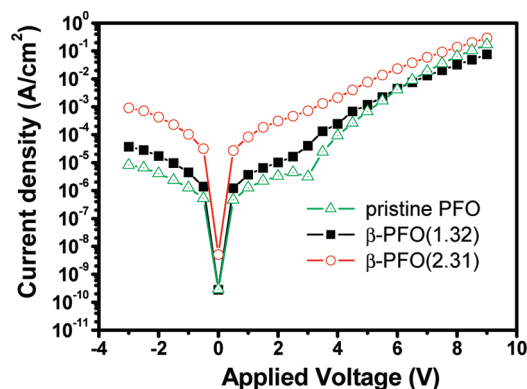


Figure 12. Current density–voltage curves of the bipolar devices with the structure: ITO/PEDOT-PSS/PFs(80 nm)/Ca(5 nm)/Al(100 nm).

a positive voltage was applied on it, the current is mainly contributed by holes (Au and ITO have work functions of around 5.1 and 5.0 eV, respectively). In our previous work,⁶⁴ we reported that the hole flux increases with increasing β -phase content (due to longer conjugating length of β -phase chains) as revealed by hole-only devices. Thus, these highly conducting regions can be attributed to the spatially inhomogeneous distribution of β -phase in PFO thin films.

3.2.2. Electrical Characteristics Study. Bipolar devices based on pristine PFO, β -PFO(1.32%), and β -PFO(2.31%) films were fabricated for studying effects of β -phase content on device performance. Devices with these films are designed as pristine PFO-device, β -PFO(1.32%)-device, and β -PFO(2.31%)-device, respectively. The characteristics of the devices are summarized in Table 3 (curves for device performance are shown in Figure S2 in the Supporting Information). The device efficiency increases as β -phase content increases to 1.32%, resulting from the special functionalities of the β -phase: electron-trapping and promoted hole mobility.⁶⁴ However, as β -phase content increases to 2.31%, the device has a lower efficiency than β -PFO(1.32%)-device. The physics behind the lower efficiency for β -PFO(2.31%)-device is revealed below. Figure 12 shows the current density–electric field curves for these devices. In the operation of reversed bias (at an applied voltage of -3 V), the current densities of pristine PFO-device, β -PFO(1.32%)-device, and β -PFO(2.31%)-device are 8.3×10^{-6} , 3.7×10^{-5} , and 9.1×10^{-4} A/cm², respectively, indicating that the leakage current increases with increasing β -phase content. The presence of leakage current reflects that the forward current could flow across the device without contributing to light emission, resulting in an energy loss and lower luminance efficiency. Therefore, the lower efficiency of β -PFO(2.31%)-device could result from a larger leakage current. The increase in β -phase content can allow an efficient energy transfer and charge trapping to occur and leads to more balanced charge fluxes and thus more efficient charge recombination.⁶⁴ However, excess content of β -phase content could also offer percolated pathways for charge transport across the PFO thin film. Thus, current can preferentially pass through these percolated pathways, which results in high-current regions in the thin film and leads to a larger current leakage and therefore lower device efficiency. Thus, the optimal content of β -phase in PFO thin film can give the device with optimal efficiency (due to a reduction of leakage current and more efficient charge recombination).

4. Conclusions

In summary, from the results of UHV-CAFM measurement on conjugated polymer thin films, we found that spatially

inhomogeneous distribution or optimal content of ordered structures in conjugated polymer thin film is also an important factor that can affect the efficiency of PLED, in addition to the other reported important factors, such as charge mobility,^{3,4,6–10,32} charge traps,³ and exciton quenching by interchain interaction,^{4,8–10,32,54,55} molecular oxygen,^{65,66} or positive polarons,⁶⁷ etc. For MEH-PPV thin films, the highly conducting regions originate from a spatially inhomogeneous distribution of nanodomains and/or aggregates. For PFO thin films, excess content of β -phase can also result in highly conducting regions. These highly conducting regions in MEH-PPV or PFO thin films can lead to a larger current leakage and therefore lower device efficiency in the corresponding PLEDs. We found for the first time that the morphology with spatially homogeneous charge transport and suppressed coverage of highly conducting regions can be achieved by a proper choice of solvent or mixed solvents for the polymer, by which the performance of PLED can be optimized (due to a reduction of leakage current).

Acknowledgment. We thank the Ministry of Education and the National Science Council for financial supports through projects 91 E-FA04-2-4A and NSC 95-2752-E007-008&005-PAE, respectively. We also thank Dr. Kang-Yung Peng for useful discussions.

Supporting Information Available: Additional experimental results on performances for MEH-PPV and PFO bipolar devices. This material is available free of charge via the Internet at <http://pubs.acs.org>.

References and Notes

- (1) Friend, R. H.; Gymer, R. W.; Holmes, A. B.; Burroughes, J. H.; Marks, R. N.; Taliani, C.; Bradley, D. D. C.; DosSantos, D. A.; Bredas, J. L.; Logdlung, M.; Salaneck, W. R. *Nature* **1999**, *397*, 121.
- (2) Heeger, A. J. *Solid State Commun.* **1998**, *107*, 673.
- (3) Liu, C. Y.; Chen, S. A. *Macromol. Rapid Commun.* **2007**, *28*, 1743.
- (4) Nguyen, T. Q.; Doan, V.; Schwartz, B. J. *J. Chem. Phys.* **1999**, *110*, 4068.
- (5) Shi, Y.; Liu, J.; Yang, Y. *J. Appl. Phys.* **2000**, *87*, 4254.
- (6) Liu, J.; Shi, Y.; Ma, L.; Yang, Y. *J. Appl. Phys.* **2000**, *88*, 605.
- (7) Liu, J.; Guo, T. F.; Shi, Y. J.; Yang, Y. *J. Appl. Phys.* **2001**, *89*, 3668.
- (8) Nguyen, T. Q.; Martini, I. B.; Liu, J.; Schwartz, B. J. *J. Phys. Chem. B* **2000**, *104*, 237.
- (9) Nguyen, T. Q.; Kwong, R. C.; Thompson, M. E.; Schwartz, B. J. *Appl. Phys. Lett.* **2000**, *76*, 2454.
- (10) Nguyen, T. Q.; Schwartz, B. J.; Schaller, R. D.; Johnson, J. C.; Lee, L. F.; Haber, L. H.; Saykally, R. J. *J. Phys. Chem. B* **2001**, *105*, 5153.
- (11) Sinha, S.; Monkman, A. P. *J. Appl. Phys.* **2003**, *93*, 5691.
- (12) Liu, C.; Zou, X. C.; Yin, S. *Jpn. J. Appl. Phys.* **2004**, *43* (4B), L563.
- (13) Inigo, A. R.; Tan, C. H.; Fann, W. S.; Huang, Y. S.; Perng, G. Y.; Chen, S. A. *Adv. Mater.* **2001**, *13*, 504.
- (14) Yang, C. Y.; Hide, F.; Diaz-Garcia, M. A.; Heeger, A. J.; Cao, Y. *Polymer* **1998**, *39*, 2299.
- (15) Lin, H. N.; Lin, H. L.; Wang, S. S.; Yu, L. S.; Perng, G. Y.; Chen, S. A.; Chen, S. H. *Appl. Phys. Lett.* **2002**, *81*, 2572.
- (16) Pingree, L. S. C.; Hersam, M. C.; Kern, M. M.; Scott, B. J.; Marks, T. J. *Appl. Phys. Lett.* **1998**, *72*, 915.
- (17) Paul, S.; Kanwal, A.; Chhowalla, M. *Nanotechnology* **2006**, *17*, 145.
- (18) Liao, Y. H.; Scherer, N. F.; Rhodes, K. J. *J. Phys. Chem. B* **2001**, *105*, 3282.
- (19) Ionescu-Zanetti, C.; Mechler, A.; Carter, S. A.; Lal, R. *Adv. Mater.* **2004**, *16*, 385.
- (20) Alexeev, A.; Loos, J.; Koetse, M. M. *Ultramicroscopy* **2006**, *106*, 191.
- (21) Alexeev, A.; Loos, J. *Org. Electron.* **2008**, *9*, 149.
- (22) Coffey, D. C.; Reid, O. G.; Rodovsky, D. B.; Bartholomew, G. P.; Ginger, D. S. *Nano Lett.* **2007**, *7*, 738.
- (23) Rappaport, N.; Solomesch, O.; Tessler, N. *J. Appl. Phys.* **2006**, *99*, 064507.
- (24) Rappaport, N.; Bar, Y.; Solomeshch, O.; Tessler, N. *Appl. Phys. Lett.* **2006**, *89*, 252117.

- (25) Athanassopoulos, S.; Kirkpatrick, J.; Martinez, D.; Frost, J. M.; Foden, C. M.; Walker, A. B.; Nelson, J. *Nano Lett.* **2007**, 7, 1785.
- (26) Chen, S. H.; Su, A. C.; Huang, Y. F.; Su, C. H.; Peng, K. Y.; Chen, S. A. *Macromolecules* **2002**, 35, 4229.
- (27) Chen, S. H.; Su, A. C.; Chou, H. L.; Peng, K. Y.; Chen, S. A. *Macromolecules* **2004**, 37, 167.
- (28) Peng, K. Y.; Chen, S. A.; Fann, W. S.; Chen, S. H.; Su, A. C. *J. Phys. Chem. B* **2005**, 109, 9368.
- (29) Collision, C. J.; Rothberg, L. J.; Treemanekarn, V.; Li, Y. *Macromolecules* **2001**, 34, 2346.
- (30) Chen, S. H.; Su, A. C.; Chang, C. S.; Chen, H. L.; Ho, D. L.; Tsao, C. S.; Peng, K. Y.; Chen, S. A. *Langmuir* **2004**, 20, 8909.
- (31) Granier, T.; Thomas, E. L.; Gagnon, D. R.; Karasz, F. E.; Lenz, R. W. *J. Polym. Sci., Part B: Polym. Phys.* **1986**, 24, 2793.
- (32) Schwartz, B. *J. Annu. Rev. Phys. Chem.* **2003**, 54, 141.
- (33) Chen, S. H.; Chou, H. L.; Su, A. C.; Chen, S. A. *Macromolecules* **2004**, 37, 6833.
- (34) Chen, S. H.; Su, A. C.; Su, C. H.; Chen, S. A. *Macromolecules* **2005**, 38, 379.
- (35) Chen, S. H.; Su, A. C.; Chen, S. A. *J. Phys. Chem. B* **2005**, 109, 10–067.
- (36) Ariu, M.; Lidzey, D. G.; Bradley, D. D. C. *Synth. Met.* **2000**, 607, 111–112.
- (37) Grell, M.; Bradley, D. D. C.; Ungar, G.; Hill, J.; Whitehead, K. S. *Macromolecules* **1999**, 32, 5810.
- (38) Hayer, A.; Khan, A. L. T.; Friend, R. H.; Köhler, A. *Phys. Rev. B: Condens. Matter Mater. Phys.* **2005**, 71, 241302.
- (39) Becker, K.; Lupton, J. M. *J. Am. Chem. Soc.* **2005**, 127, 7306.
- (40) Khan, A. L. T.; Sreearunothai, P.; Herz, L. M.; Banach, M. J.; Köhler, A. *Phys. Rev. B: Condens. Matter Mater. Phys.* **2004**, 69, 085201.
- (41) Yu, L. S.; Chen, S. A. *Adv. Mater.* **2004**, 16, 744.
- (42) Hung, M. C.; Liao, J. L.; Chen, S. A.; Chen, S. H.; Su, A. C. *J. Am. Chem. Soc.* **2005**, 127, 14576.
- (43) Johnson, K. L. *Contact Mechanics*; Cambridge University Press: Cambridge, UK, 1985.
- (44) From the Hertz model, we have $a^3 = 3FR/4Y^*$ and $1/Y^* = (1 - \nu_1^2)/Y_1 + (1 - \nu_2^2)/Y_2$, where a is contact radius, F the load, R the tip radius, Y Young's modulus, and ν the Poisson's ratio. With 20 nN, $R = 50$ nm, $Y_1 = 81$ GPa, $\nu_1 = 0.42$ (for Au), and $Y_2 = 3$ GPa, $\nu_2 = 0.35$ (for MEH-PPV), a is calculated to be around 6.1 nm.
- (45) Huo, L.; Hou, J.; He, C.; Han, M.; Li, Y. *Synth. Met.* **2006**, 156, 276.
- (46) Chen, M. C.; Chen, S. A. *Thin Solid Films* **2009**, 517, 2708.
- (47) Kim, K. B.; Tak, Y. H.; Han, Y. S. K.; Baik, H.; Yoon, M. H.; Lee, M. H. *Jpn. J. Appl. Phys.* **2003**, 42, L438.
- (48) Ke, L.; Chua, S. J.; Zhang, K.; Yakovlev, N. *Appl. Phys. Lett.* **2002**, 80, 2195.
- (49) Jeng, U.; Hsu, C. H.; Sheu, H. S.; Lee, H. Y.; Inigo, A. R.; Chiu, H. C.; Fann, W. S.; Chen, S. H.; Su, A. C.; Lin, T. L.; Peng, K. Y.; Chen, S. A. *Macromolecules* **2005**, 38, 6566.
- (50) Li, Y. C.; Chen, K. B.; Chen, H. L.; Hsu, C. S.; Tsao, C. S.; Chen, J. H.; Chen, S. A. *Langmuir* **2006**, 22, 11009.
- (51) Sirringhaus, H.; Brown, P. J.; Friend, R. H.; Nielsen, M. M.; Bechgaard, K.; Langeveld-Voss, B. M. W.; Spiering, A. J. H.; Janssen, R. A. J.; Meijer, E. W.; Herwig, P.; Leeuw, D. M. D. *Nature* **1999**, 401, 685.
- (52) Kline, R. J.; McGehee, M. D.; Kadnikova, E. N.; Liu, J. S.; Frechet, J. M. J. *Adv. Mater.* **2003**, 15, 1519.
- (53) Chang, J. F.; Sun, B. Q.; Breiby, D. W.; Nielsen, M. M.; Solling, T. I.; Giles, M.; McCulloch, I.; Sirringhaus, H. *Chem. Mater.* **2004**, 16, 4772.
- (54) Peng, K. Y.; Chen, S. A.; Fann, W. S. *J. Am. Chem. Soc.* **2001**, 123, 11388.
- (55) Martens, J. H. F.; Bradley, D. D. C.; Burn, P. L.; Friend, R. H.; Holmes, A. B.; Marseglia, E. A. *Synth. Met.* **1991**, 301, 41–43.
- (56) Martens, J. H. F.; Marseglia, E. A.; Bradley, D. D. C.; Friend, R. H.; Burn, P. L.; Holmes, A. B. *Synth. Met.* **1993**, 449, 55–57.
- (57) Yan, M.; Rothberg, L. J.; Papadimitrakopoulos, F.; Galvin, M. E.; Miller, T. M. *Phys. Rev. Lett.* **1994**, 73, 744.
- (58) Jakubiak, R.; Collision, C. J.; Wan, W. C.; Rothberg, L. J.; Hsieh, B. R. *J. Phys. Chem. A* **1999**, 103, 2394.
- (59) Schaller, R. D.; Snee, P. T.; Johnson, J. C.; Lee, L. F.; Wilson, K. R.; Haber, L. H.; Saykally, R. J.; Nguyen, T. Q.; Schwartz, B. J. *J. Chem. Phys.* **2002**, 117, 6688.
- (60) Huser, T.; Yan, M. *Synth. Met.* **2001**, 116, 333.
- (61) Tan, C. H.; Inigo, A. R.; Fann, W. S.; Wei, P. K.; Huang, Y. S.; Perng, G. Y.; Chen, S. A. *Org. Electron.* **2002**, 3, 81.
- (62) Tan, C. H.; Inigo, A. R.; Hsu, J. H.; Fann, W. S.; Wei, P. K. *J. Phys. Chem. Solids* **2001**, 62, 1643.
- (63) Tseng, H. E.; Liu, C. Y.; Chen, S. A. *Appl. Phys. Lett.* **2006**, 89, 233510.
- (64) Lu, H. H.; Liu, C. Y.; Chang, C. H.; Chen, S. A. *Adv. Mater.* **2007**, 19, 2574.
- (65) Yu, J.; Hu, D.; Barbara, P. F. *Science* **2000**, 289, 1327.
- (66) Park, S. J.; Gesquiere, A. J.; Yu, J.; Barbara, P. F. *J. Am. Chem. Soc.* **2004**, 126, 4116.
- (67) Yu, J.; Song, N. W.; McNeill, J. D.; Barbara, P. F. *Isr. J. Chem.* **2004**, 44, 127.

JP901644M